Applied Surface Science 552 (2021) 149428

Contents lists available at ScienceDirect

Applied Surface Science

journal homepage: www.elsevier.com/locate/apsusc

Full Length Article

Solar-triggered photothermal therapy for tumor ablation by Ag nanoparticles self-precipitated on structural titanium oxide nanofibers

Ting-Han Lin [a], Ming-Chung Wu [a,b,c,*], Yen-Ting Lin [a], Chi-Hui Tsao [d], Yin-Hsuan Chang [a], Kou-Ping Chiang [a], Yu-Ting Huang [e], Yu-Jen Lu [e,f,**]

[a] Department of Chemical and Materials Engineering, College of Engineering, Chang Gung University, Taoyuan 33302, Taiwan
[b] Green Technology Research Center, Chang Gung University, Taoyuan 33302, Taiwan
[c] Division of Neonatology, Department of Pediatrics, Chang Gung Memorial Hospital, Linkou, Taoyuan 33305, Taiwan
[d] Department of Biomedical Sciences, College of Medicine, Chang Gung University, Taoyuan 33302, Taiwan
[e] Department of Neurosurgery, Chang Gung Memorial Hospital, Linkou, Taoyuan 33305, Taiwan
[f] College of Medicine, Chang Gung University, Taoyuan 33302, Taiwan

ARTICLE INFO

Keywords:
Hydrothermal synthesis
Ag self-precipitation
Solar triggered
Photothermal therapy

ABSTRACT

Photothermal therapy is considered to be a promising approach for minimally invasive tumor treatment. Before the clinical trial, the photo-induced heat production efficiency in tumor tissue needs improvement. Herein, we demonstrated a one-pot hydrothermal synthesis followed by calcination to prepare the Ag NPs-precipitated TiO_2 photocatalysts. With calcination temperature ascending, anatase TiO_2 transformed into rutile TiO_2, and self-precipitated Ag NPs vanished. Besides, fibers started to sinter with adjacent fibers, transforming into the bulk form. Due to the rich Ag NPs precipitated on the surface, leading to strong surface plasma resonance, Ag doped anatase TiO_2 NFs (STF) presented the superior photocatalytic activity. Under the irradiation, 10,000 ppm of STF showed significant temperature enhancement in the photothermal conversion in vitro and the photothermal therapy in vivo. The body surface temperature can be increased up to 47.96 °C with an irradiation time of 5.0 min. Moreover, the tumor growth was inhibited for up to 24 days, and the survival rate of mice was extended. From the protein identification of HE and Caspase 3 stain, STF proficiently disturbed the tumor expansion and led to tumor cell apoptosis. STF triggered by xenon lamp irradiation contributed to the significant tumor ablation and showed great potential in photothermal therapy.

1. Introduction

Breast cancer has been a huge threat to women's health. Statistics show that about 12% of U.S. women develop invasive breast cancer [1]. Photothermal therapy is a treatment relying on optical absorbing agents, which convert photon energy into heat to induce hyperthermia [2–4]. Compared to traditional therapies, such as chemotherapy and ionizing radiotherapy, photothermal therapy has emerged as a promising approach due to its minimal invasiveness, enhanced therapeutic effect, reduced side effect, and high safety [5–7]. For cancerous tissues, a sufficiently high temperature of 40~50 °C is needed to kill tumor cells [8–10]. As an efficient photothermal agent, it should not be triggered by UV irradiation considering the limitation of UV penetration (<1.0 mm) and the adverse side-effects an excessive dose can induce [11–13]. To the best of our knowledge, TiO_2 as photocatalyst shows the ability to generate reactive oxygen species (ROS) for photodynamic therapy. The inherent properties such as biocompatibility, high chemical stability all contribute to it being an effective photo-response agent [14,15]. However, there exist some issues which hinder its biomedical application.

It has been demonstrated that TiO_2 has a wide range of applications, such as photovoltaic cells [16,17], photochemistry [18,19] and photocatalysts [20,21], due to the fascinating optical properties of TiO_2. However, its wide bandgap (>3.2 eV) with its responsiveness to UV strongly inhibits the potential in phototherapy. After the UV photothermal therapy, it may result in skin damage. Therefore, considerable effort has been devoted to enhance the light absorption of TiO_2 for efficient utilization of the visible light energy spectrum [22]. Surface defective engineering of TiO_2 by hydrogenation elicited apparent

* Corresponding author at: Department of Chemical and Materials Engineering, College of Engineering, Chang Gung University, Taoyuan 33302, Taiwan.
** Corresponding author at: Department of Neurosurgery, Chang Gung Memorial Hospital, Linkou, Taoyuan 33305, Taiwan.
E-mail addresses: mingchungwu@cgu.edu.tw (M.-C. Wu), luyj@cgmh.org.tw (Y.-J. Lu).

https://doi.org/10.1016/j.apsusc.2021.149428
Received 30 October 2020; Received in revised form 13 February 2021; Accepted 25 February 2021
Available online 2 March 2021

improvement of absorption ranged from visible to near-infrared [14,23,24]. Incorporation of visible absorbing materials and heterogeneous element doping strategy has been extensively studied to construct hetero-surface structures and to modify the electronic structure, which impedes electron-hole recombination [25,26]. These changes allow for effective photo-response under visible light irradiation.

Based on our best knowledge and investigation, silver doped TiO_2 nanofibers has been employed to extend the absorption threshold, and the surface plasma resonance (SPR) induced by silver can lead to the enhancement of light absorption [27,28]. Remarkably, silver ions are either incorporated into crystal lattice or intercalation or highly dispersed on the surface of TiO_2 as pure metal clusters during the calcination process. This is due to the difference of Gibb's free energy between silver and titanium. The photothermal effect may further facilitate the mobility of photo-induced charge carriers, thus preventing the recombination, attributing to the heterostructure construction.

In this study, we demonstrated a one-pot hydrothermal method combined with simple air calcination to prepare various TiO_2 NFs with tunable crystal structure and surface modification. By introducing the surface plasma resonance, we further incorporated silver dopants to TiO_2 NFs and identified their surface precipitation effect on TiO_2 NFs surface. With the optimal calcination process, it was feasible to control the crystal structure transformation and the surface precipitation of silver ion to nanoparticles at the same time. Among them, Ag-doped anatase TiO_2 NFs (STF) performed the optimal photoresponse due to SPR enhancement of absorption. It was also used as an agent in photothermal therapy (PTT), revealing a significant temperature increase in vitro. During in vivo experiments, mice treated with STF possessed outstanding behavior in every survival factors. It is also dedicated to the biocompatibility of STF and its effectual photothermal effect on the 4T1 tumor cell apoptosis.

2. Experimental section

2.1. Synthesis of photocatalysts

Anatase TiO_2 NFs were prepared by a one-pot hydrothermal method and further calcined in the air. Anatase TiO_2 powder (Acros, 98+%, Belgium) with a weight of 25.0 g was chosen as the raw material and reacted with 625.0 ml of 10.0 M sodium hydroxide (NaOH, Fisher Scientific, >97%, USA) solution for 24 h in a 1,000 cm^3 self-designed Teflon-lined autoclave. The obtained sodium titanate nanofibers were repeatedly washed with deionized water and diluted hydrochloric acid (HCl, Acros, 37%, Belgium) until a neutral solution was obtained. After drying, the hydrogen titanate nanofibers were calcined at 600 °C in the air atmosphere to obtain Anatase TiO_2 NFs. For the synthesis of silver doped TiO_2 NFs, we followed the as-mentioned hydrothermal method with added silver nitrate ($AgNO_3$, Choneye Pure Chemicals, extra pure, Taiwan) at a molar ratio of 5.0 mol% to the mixture of anatase TiO_2 powder and NaOH. After the hydrothermal and washing process, Ag-doped hydrogen titanate NFs was further calcined at 600, 800, and 1000 °C, to attain various Ag-doped TiO_2 NFs. We named the Ag-doped TiO_2 calcined at 600, 800, and 1000 °C as Ag/A-TiO_2 NFs (STF), Ag/A-TiO_2 NRs (STR), and Ag/R-TiO_2 bulks (STB), respectively. This was based on the morphological observation and identification of crystal structure, where A and R mean the anatase and rutile phases, respectively. The summarized information of as-prepared samples is presented in Table S1.

2.2. Material characterization

The morphology was investigated by field-emission scanning electron microscope (FESEM, SU8010, Hitachi, Japan) and spherical-aberration corrected field-emission transmission electron microscope (FETEM, JEM-ARM200FTH, JEOL, Japan). The UV–VIS absorption spectra were recorded by the UV–VIS spectrophotometer (1900i, Shimazu, Japan) with a scan rate of 400 nm·min^{-1} and a data interval of 1.0 nm. The X-ray spectra were performed by synchrotron X-ray spectroscopy (λ ~ 1.025 Å) on beamline 13A1 of the National Synchrotron Radiation Research Center (NSRRC) in Taiwan and recorded from 2θ between 5° to 45° with a 0.01° step at 0.02°·s^{-1}. To unveil the silver loaded on TiO_2 NFs, we used a photoelectron spectrometer with an X-ray source of Al Kα (K-alpha X-ray photoelectron spectrometer, Thermo Fisher Scientific, USA) to scan the Ag 3d orbital for elemental analysis.

2.3. Photocatalytic experiment

In the photodegradation experiment of hydroquinone (Acros, 99.5%, Belgium), 20.0 mg of the photocatalyst was dispersed in the 1.0 ppm of aqueous hydroquinone. To minimize the influence of adsorption, the suspension was stirred for 60 mins in the dark. The degradation was conducted at room temperature and at a consistent pH value, which is around 7. Afterward, the suspension was irradiated to two visible lamps (Philips, TWG206 TL5/14 W) at ambient conditions under continuous stirring. With the time intervals, 3.0 ml of suspension was sampled and further centrifuged for 15 min at 5000 rpm. The remaining concentration of hydroquinone in the supernatant was calculated by the absorption spectrum, which was recorded by the UV–VIS spectrophotometer (V-730, JASCO, Japan) in the 250–600 nm. The relevant rate constant was derived by $\ln(C_0/C) = kt$, where k is the apparent reaction rate constant. *p*-Benzoquinone (Acros, 99%, Belgium), ammonia oxalate ((VETEC, 98%, trademark of Sigma-Aldrich, USA), and *tert*-Butyl alcohol (J.T.Baker, ≥99.0%, USA) were used as scavengers for the detection of reactive oxygen species, which captured the superoxide radicals, holes, and hydroxyl radicals, respectively.

2.4. In vitro and in vivo experiment

For the photothermal conversion in vitro, STF agent was prepared by well-dispersed STF into 0.1 ml of phosphate-buffered saline (PBS, pH = 7.4). The phosphate-buffered saline, and 5000, 10000, 15000 ppm of STF agents were further illuminated under a 300 W xenon lamp (PLS-SXE300, perfectlight, china) for 300 s. The real-time temperature for agents was recorded by a thermal couple thermometer (Hanna Instruments, Woonsocket, RI, USA). The biocompatibility of TiO_2 NFs was performed by subcutaneously injecting TiO_2 agent into the abdominal cavity of Blab/c mice (National Laboratory Animal Center). For the photothermal therapy in vitro, fifteen female Blab/c mice, each with breast tumor cells, 4T1 cells, and volume reaching 270 mm^3, were randomly assigned to on control group and two experiment groups (n = 5). The tumor-bearing mice were injected with 100 mg·kg^{-1} per week. After the intratumoral injection of 0.1 ml of STF agent, the mice were illuminated under a 300 W xenon lamp for 300 s. The thermal profiles of tumor-bearing mice were captured by an infrared thermal image camera (T530, FLIR, USA) to recognize the temperature distribution. The body weight and tumor volume were monitored every day. As the tumor volume exceeded 1000 mm^3, mice were put down, and the tumors were collected in 10% buffered formalin for Hematoxylin and eosin (HE) protein, KI67 protein, and caspase 3 determination.

3. Results and discussion

3.1. Photocatalyst characterization

To reveal the morphological transformation during the calcination process, we fabricated the anatase TiO_2 NFs and Ag-doped TiO_2 NFs with various calcination temperatures. We also studied the surface precipitation of silver dopants. We first conducted various electronic microscopies, including FESEM and FETEM. In Fig. 1(a-d), the as-synthesized TiO_2 NFs was used as a reference, showing the uniform surface and fibers like structure (Fig. 1(a)). When the silver dopant was incorporated with TiO_2 in the hydrothermal reaction and further calcined at 600 °C,

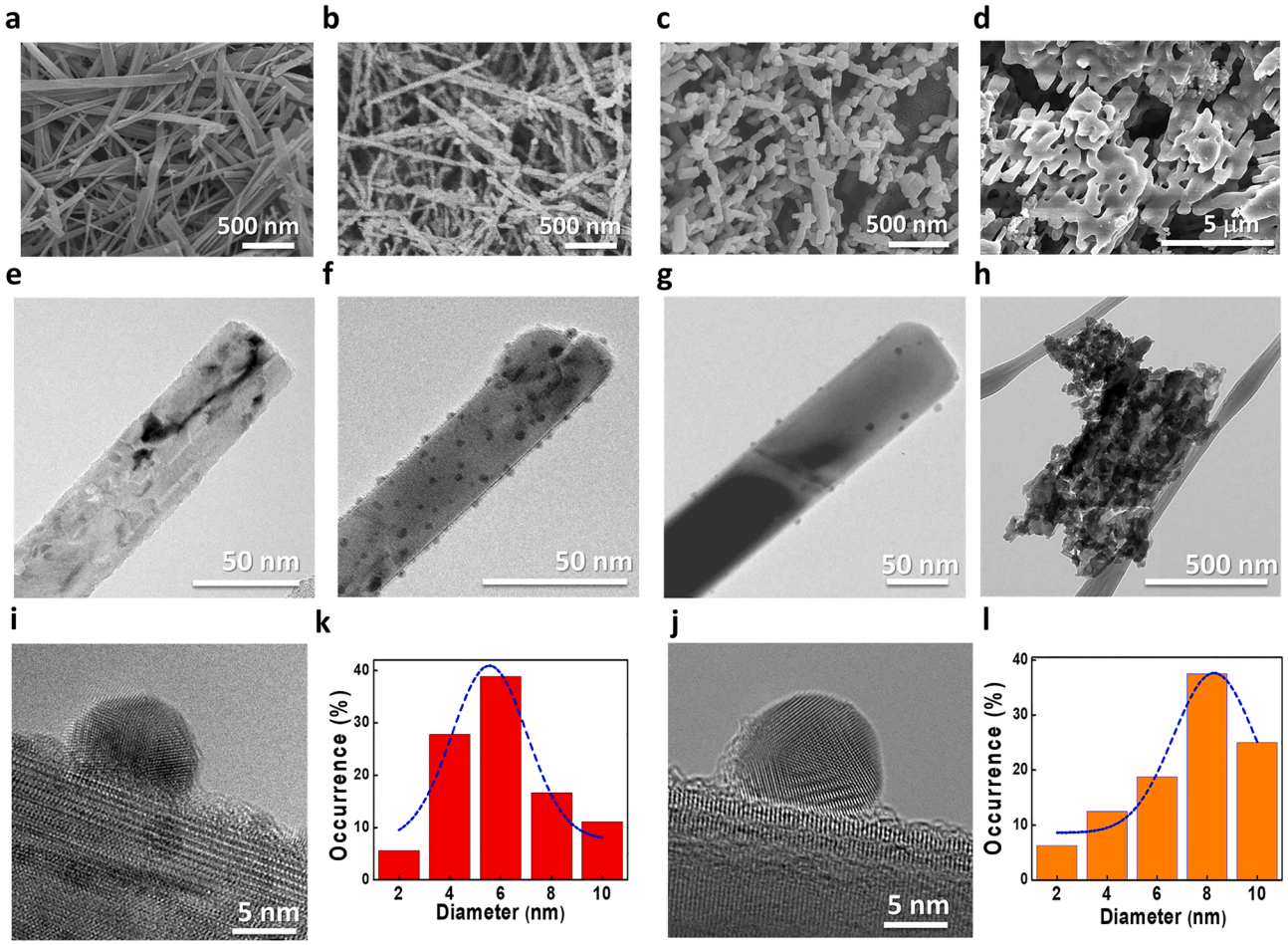

Fig. 1. FESEM and FETEM images of (a,e) anatase TiO_2, and Ag-doped TiO_2 calcined at (b,f) 600 °C, (c,g) 800 °C, and (d,h) 1000 °C; magnified TEM image of Ag-doped TiO_2 calcined at (i) 600 °C and (j) 800 °C, and related size distribution,(k) 600 °C and (l) 800 °C.

the fibers-like structure was presented as anatase TiO_2 NFs, but it might be transformed into a rods-like structure at a calcination temperature of 800 °C (Fig. 1(b,c)). The nanofibers and nanorods started to sinter as the calcination temperature ascended to 1000 °C, becoming the TiO_2 bulks (Fig. 1(d,h)). In the FETEM observation, anatase TiO_2 NFs and Ag-doped TiO_2 NFs calcined at 600 °C presented an average diameter of 50 and 30 nm, respectively (Fig. 1(e,f)). Remarkably, several Ag NPs appeared and precipitated on the TiO_2 surface. In the magnified TEM image (Fig. 1(i)), silver NPs not only located on the surface but also embedded in the nanofibers, suggesting the silver dopants diffused from the core to the shell. Moreover, as consistent as the SEM observations showed, Ag-doped TiO_2 calcined at 800 °C possessed 2.5 times larger diameter, which was around 80 nm. From the TEM and SEM observation, it was suggested that it shrunk and became rods like structure (Fig. 1(g)). The number of Ag NPs decreased apparently, and their average size increased (Fig. 1(j)). It was suggested that Ag dopants kept growing up in the same seed, but the formed Ag NPs might be decomposed during the calcination due to low thermal stability. The average sizes of Ag NPs on Ag-doped TiO_2 calcined at 600 °C and 800 °C were 5.9 nm and 7.4 nm, and their size distributions are shown in Fig. 1(k,l). Base on these observations, we named the anatase TiO_2 NFs, Ag-doped TiO_2 calcined at 600, 800, and 1000 °C as ATF, STF, STR, and STB, respectively

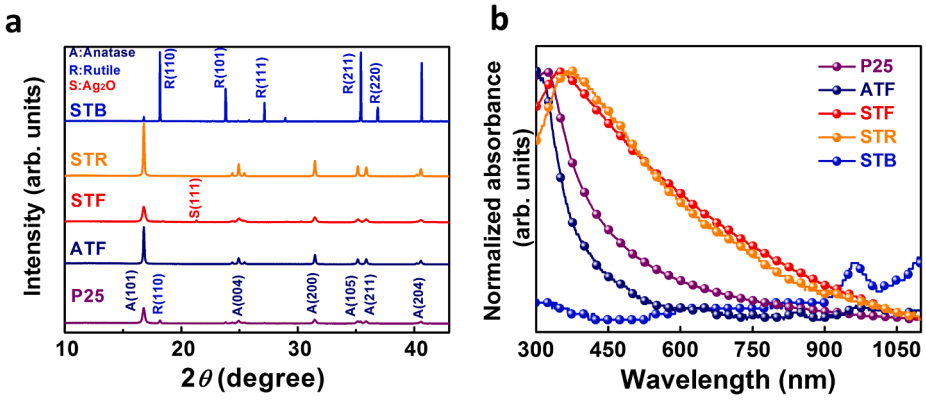

Fig. 2. (a) Synchrotron X-ray scattering spectra and (b) absorption spectra of various TiO_2 photocatalysts.

(Table S1).

The crystal structure plays a vital role in the 1-D TiO_2 materials, dominating the ability and efficiency of charge transport. We determined their crystalline properties using synchrotron X-ray scattering spectroscopy. (Fig. 2(a)) According to JCPDS No. 00-021-1272, the typical diffraction of the anatase phase can be indexed in the spectra of ATF, and assigned to (101), (004), (200), (105), (211), (204), (116), (220), and (215) plane. Both STF and STR revealed the consistent reflection plane in the spectra, but the latter showed higher intensity than the former due to high crystalline enhanced by high-temperature annealing. The silver derivates were also observed in the spectra of STF, indicating much more Ag NPs precipitated on the surface. Notably, the crystal structure of STB showed the rutile phase mainly, and their reflection planes can be assigned to (110), (101), (111), (211), and (220). (JCPDS No. 21-1276) It was concluded that as calcination temperature reached higher than 1000 °C, the anatase phase transformed into the rutile phase. In general, the anatase phase is desired in the photocatalytic reaction due to efficient transport behavior. The construction of heterostructure also provided a pathway to inhibit the electron-hole recombination, leading to higher activities in the photo-induced reaction.

The optical property is the essential factor in deciding the catalyst's photoresponse. From the EM results, we observed that silver dopants presented the self-precipitation effect during the air calcination, and TiO_2 nanofibers transform to nanorod and further to bulks. As silver dopants migrated to the surface, in the form of nanoparticles, it might contribute to a significant change in absorption properties. Herein, we demonstrated their absorption spectra (Fig. 2(b)). ATF and P25 showed the photo-responses only in the range of the ultraviolet region. STB presented a low absorbance, showing little light diffusing through in the near IR region due to large-sized bulks not allowing the light passing through. Both STF and STR exhibited the broad absorbance in the visible region, suggesting the successful surface medication caused by surface plasma resonance of silver NPs. The silver-inducing surface plasma resonance is coupled with the intrinsic light absorption, improving the strong absorption.

To evaluate the photocatalytic activity, we conducted the photodegradation of hydroquinone using various TiO_2 photocatalysts. Compared to the commercial Aeroxide® P25 photocatalyst, ATF and STF showed more efficient photodegradation toward the hydroquinone (Fig. 3(a)). It was because of high crystalline of the anatase phase, improving the charge transport in the TiO_2. The silver incorporation also enhanced the absorption properties in the visible region due to surface plasma resonance caused by self-precipitated Ag NPs. Through the first-order linear transform from C/C_0 (Fig. 3(b)), the rate constant of STF reached as high as 0.00126 min^{-1} (Fig. 3(c)). However, STR and STB presented even lower activities than P25. It was suggested that raising temperature to 800 °C induced shrinking and sintering fibers, lowering the specific surface area. Meanwhile, from the microstructure observation, surface-precipitated Ag NPs gradually vanished and were practically missing at a calcination temperature of 1000 °C. It is attributed to the evaporation of Ag NPs and the derivatives as the calcination temperature is close to the melting point of 961 °C or higher. The SPR enhancement did not occur, dramatically reducing the degradation activity. Thus, we considered the STF was the most potential candidate and used it for further investigation.

The reactive oxygen species generated by STF were examined using various scavengers in the photodegradation (Fig. 4). The various scavengers, including *p* -Benzoquinone, ammonia oxalate, and *tert*-butyl alcohol, were capable of capturing the photogenerated electrons, holes, and hydroxide radicals, respectively. With *tert*-butyl alcohol, the photodegradation activity was slightly disturbed due to the low level of hydroxide radicals evolution. In the ammonia oxalate experiment, its photocatalytic activity showed better than the former, indicating the more holes led to the discoloration. As incorporated with *p*-benzoquinone, strong inhibition of photodegradation was observed, indicating the rich electrons dominated the activity. It is noted that the electrons migrated successfully from the core to the interface due to the constructed heterostructure of self-precipitated silver nanoparticles. It contributed to promote electron migration and to prolong the carriers' life on the Ag NPs. Therefore, STF not only showed remarkable photoresponse in the visible region but also possessed the understanding ability to generate the electron in the photo-induced reaction. We chose STF for further study.

3.2. Cytotoxicity evaluation in vivo

For the photothermal therapy investigation, we first evaluated the

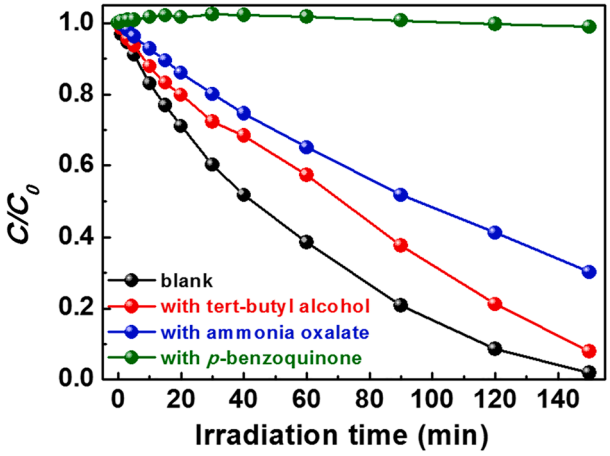

Fig. 4. Photodegradation of STF with various scavengers, including *tert*-butyl alcohol, ammonia oxalate, *p*-benzoquinone.

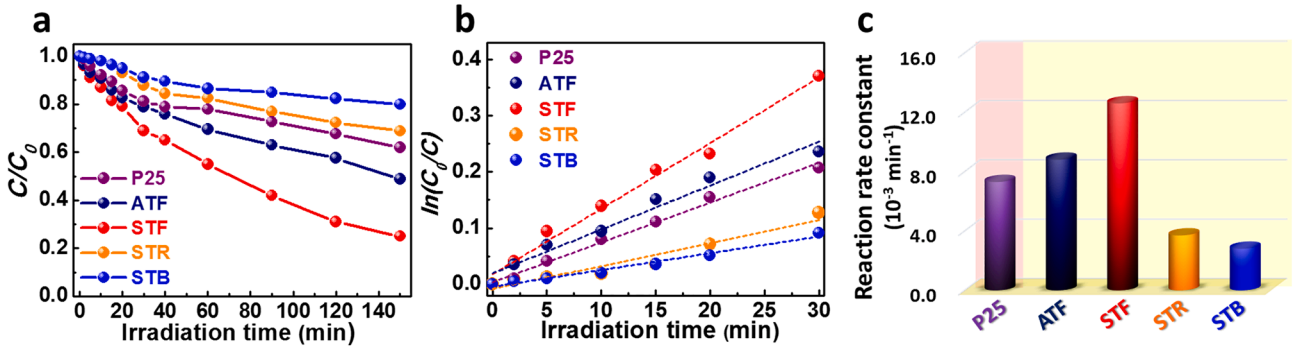

Fig. 3. (a) Photocatalytic degradation, (b) the apparent first-order linear transforms, and (c) the comparison chart of the hydroquinone degradation rate of various TiO_2 photocatalysts under the visible irradiation.

biocompatibility of TiO_2 nanofibers in vivo through the subcutaneous injection to the abdominal cavity of Blab/c mice. From the periodic observation over a period of one month (Fig. 5), mice maintained the expected behavior of eating, drinking, excretion, and neurological status. Furthermore, the organs, including the heart, liver, kidney, lung, and pancreas, were investigated after the mice were put down. Compared to the control group with saline injection, the tissue in every organ displayed an equal status. It was suggested that the presence of TiO_2 nanomaterial in vivo was not damaging any tissues in the organs or causing necrosis, inflammation, or pulmonary fibrosis in mice.

3.3. Photothermal conversion in vitro

The proficiency of photothermal conversion in vitro tests depends on the absorption of the photocatalyst in the visible and near-infrared region. Under the continuous xenon lamp illumination, the surrounding temperature of the 4T1 cell in the saline increased around 2.0 °C due to the slight absorption of the cell medium and the strong thermal radiation effect of near-infrared (Fig. 6 (black)). Compared to the control experiment of the 4T1 cell in the saline, the cell temperature in the presence of various STF doses showed a significant increase under irradiation. Moreover, the temperature can be boosted up to 34 °C as the doses of STR increased to 10,000 ppm (Fig. 6 (green)) and 15,000 ppm (Fig. 6 (red)). As the photocatalyst dose in the PTT agent raised to above 10,000 ppm, the temperature maintained at a similar level. It indicated the saturated dose has been achieved, and excessive suspension in the medium has not helped increasing the absorption. Thus, 10,000 ppm in the STF agent was the optimal concentration for the further PTT experiment.

3.4. Photothermal therapy in vivo

STF not only exhibited excellent proficiency in vitro, but also showed the biocompatibility in vitro. It is plausible for it to be an agent injected into the tumor-bearing mice for photothermal therapy. Herein, we carried out the PTT treatment under the xenon irradiation also demonstrated its solar-driven ability. Fifteen female mice, each with tumor volume reaching 270 mm^3, were randomly assigned to one control group and two experimental groups (n = 5). The control group was injected with saline, and the STF group was only injected with 100 $mg{\cdot}kg^{-1}$ into mice. Before the surgery of photothermal therapy, mice were anesthetized by isoflurane and subsequently exposed to Xe lamp irradiation. Fig. 7 presented the photothermal images of the 4T1 tumor site on mice injected with saline and STF. With continuous irradiation of the Xe lamp for 5 min, the temperature on the tumor site (black circle) in the STF group raised rapidly up to 47.96 °C, but that in the control group merely increased, attaining to a temperature of 40.45 °C (Fig. 7(a,b)). Although Xe lamp irradiation led to a large area exposure, the tumor site injected with STF revealed a significant enhancement of surface

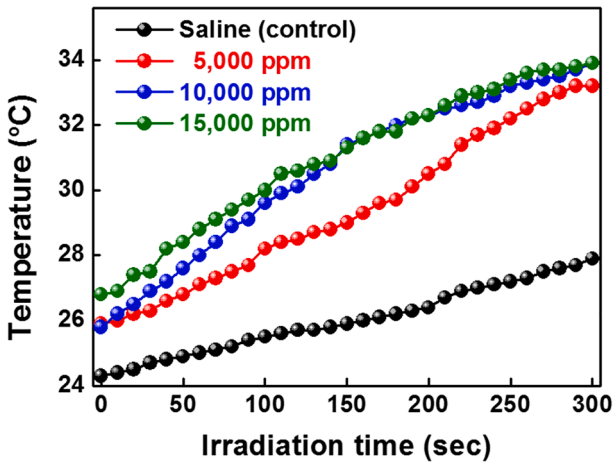

Fig. 6. In vitro test for photothermal conversion proficiency at different concentration; 5,000 ppm (red), 10,000 ppm (blue), 15,000 ppm (green). (For interpretation of the references to colour in this figure legend, the reader is referred to the web version of this article.)

temperature at a specific area under irradiation. The relevant temperature of tumor sites in the mice body surface over the irradiation times was recorded (Fig. 7(c)). Notably, the injection of STF raised the temperature from 36 to 45 °C within 3 min, and the relevant temperature change was around 10 °C during the PTT treatment. On the contrary, the control group with the injection of saline showed minor change caused by the thermal radiation of the Xe lamp. Based on general knowledge for photothermal therapy, it is believed that the body surface temperature, which is higher than 40 °C, is capable of tumor ablation. The result was expected given the feasibility of STF applied to the PTT in vivo.

To validate the proficiency of STF for photothermal therapy on tumor ablation, we injected the STR agent on the first and eighth day and conducted the irradiation every day. After the daily treatment, the tumor volumes of mice were monitored as the indices for the evaluation of survival. The body weights of mice were also collected among groups every two days. The tumor volume was estimated by the following equation:

$$\text{Tumor volume } (mm^3) = \frac{\text{length (mm)} \times (\text{width(mm)})^2}{2} \quad (1)$$

When the volume of the tumor reached 1,000 mm^3, mice were put down, and their tumors were collected for further analysis. Herein, we divided the in vivo experiment into three treatment groups as the control group injected with saline and experimental STF injected groups with and without xenon lamp illumination. The average tumor volume and body weight of mice were presented in Fig. 8. The mice's tumor volume in the control group and the STF group without illumination grew large

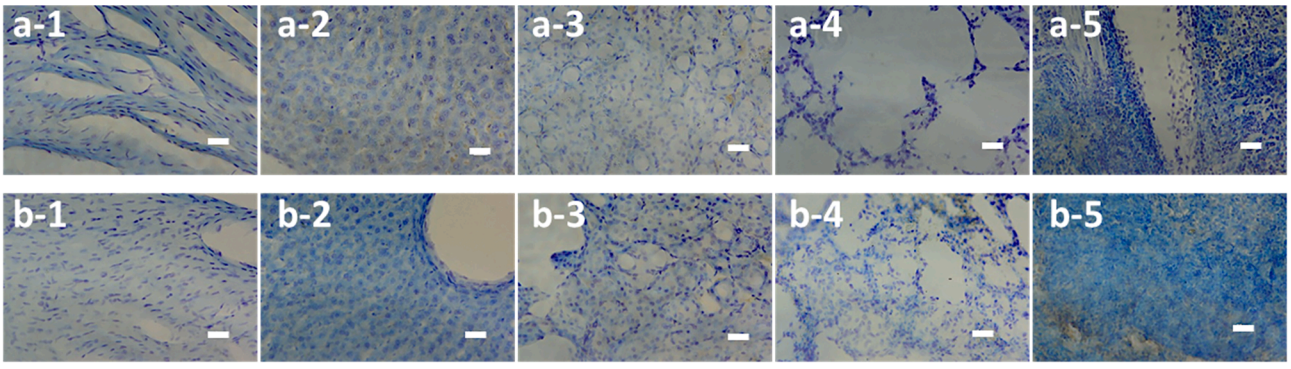

Fig. 5. Microscope images of mice organs including (□-1) heart, (□-2) liver, (□-3) kidney, (□-4) lung, and (□-5) pancreas, injected by saline as (a-□) control and (b-□) TiO_2 nanofibers. (scale bar = 30 μm).

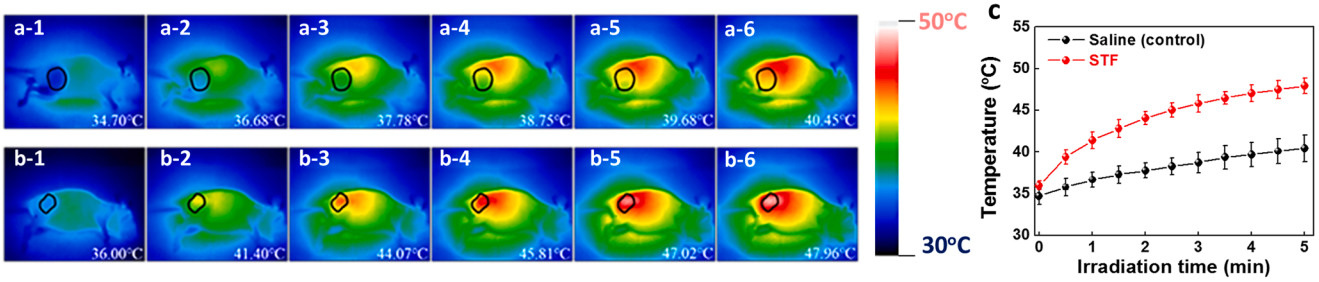

Fig. 7. Photothermal images of 4T1 tumor site on mice injected with (a-□) saline (control) and (b-□) STF agent under the Xe lamp irradiation at (□-1) 0 min, (□-2) 1 min, (□-3) 2 min, (□-4) 3 min, (□-5) 4 min, and (□-6) 5 min ; (c) average temperature of tumor sites in body surface of mice.

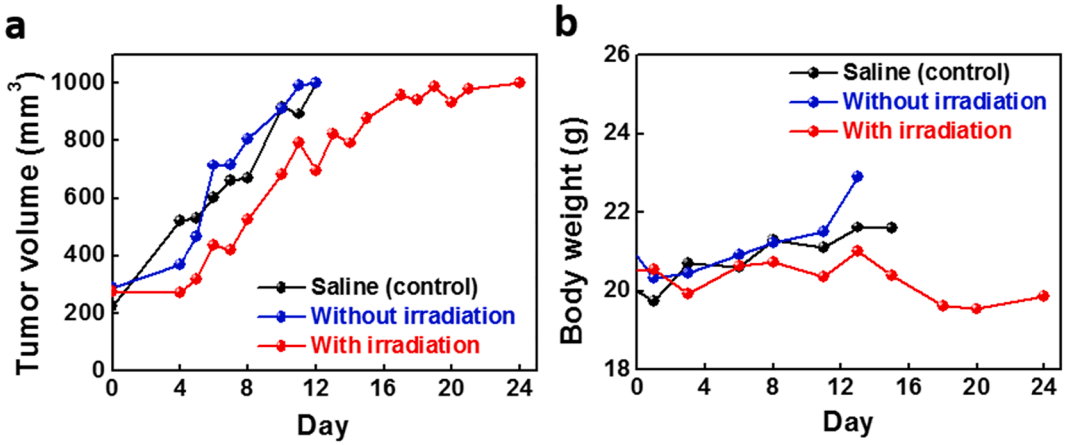

Fig. 8. In vivo test for the photothermal therapeutic effect on (a) tumor volume, and (b) body weight under Xe lamp irradiation.

and exceeded the 1,000 mm^3 on the 12th day. It has been determined that STF was not triggered without any irradiation, but showed its non-toxicity to mice comparing to the control group. On the contrary, the STF injection group with irradiation inhibited the excessive tumor growth, which was reflected on volume change. The procedure kept the average tumor volume below the volume threshold. The efficient inhibition of tumor growth was attributed to the sufficient photothermal conversion of STF. It was also convinced that SPR enhanced STF possessed outstanding ability to convert the solar energy to thermal radiation or conduction, further ablated the tumor cell due to the feasible temperature (>45 °C) [8,9]. From the bodyweight analysis, we observed that the weight change of the control and STF without irradiation group increased slightly due to the tumor growth, which dominated the nutrition absorption of daily meals. In contrast, STF with irradiation group maintained the body weight near the 20.0 g during the 24 days observation.

The profiles of the survival rate of tumor-bearing mice were demonstrated in Fig. 9. Similar to the tumor volume analysis, most of the mice in the control group and STF group without irradiation started to pass away, and others were sacrificed due to unreasonable tumor volume in 12 days. Remarkably, over half of the mice in the STF with the irradiation group survived for over 16 days, and the remaining mice even prolonged survival to the 24th day. It was two times longer than that of control group and STF group without irradiation. In summary, STF performed superior photothermal conversion under xenon lamp illumination in vitro and in vivo, further enhancing the solar-triggered tumor ablation's proficiency.

To clarify the tumor ablation caused by the photothermal effect of STF, we further carried out the histological protein stain analysis after the mice were put down. Several standard proteins involving Hematoxylin and eosin (HE) protein, KI67 protein, and caspase 3 protein were stained in vitro for the tumor cell behavior after the photothermal

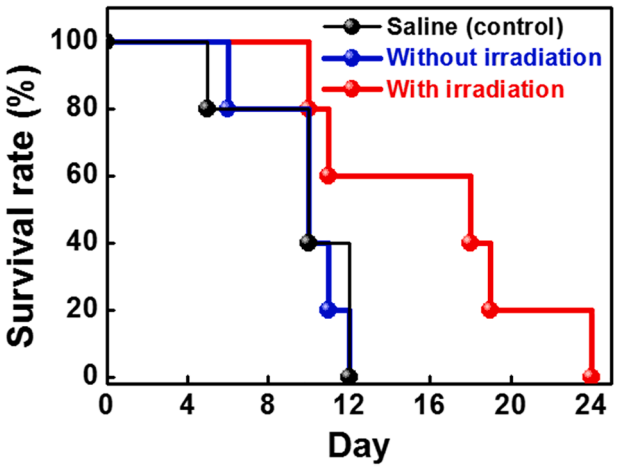

Fig. 9. The survival rate of bearing-tumor mice during photothermal therapy.

therapy (Fig. 10). The indication of KI67 protein was helpful for revealing the active proliferation, usually identifying a tumor cell (Fig. 10 (□-1)). From the protein analysis of three groups, they presented a consistent result, suggesting that tumor cells had been grown in the mice. In the HE stain analysis (Fig. 10 (□-2)), the purple dots and pink dots referred to the nucleus and cytoplasm of alive tumor cells. It presented the dramatic difference in tumor cell numbers in various groups. STF group with irradiation showed the fewest cells compared to the control group and STF group without irradiation, suggesting most of the tumor cells has undergone apoptosis. Moreover, Caspase 3 was an indicator to catch the transmitter during the cell autophagy (Fig. 10 (□-3)). In the case of the STF group with irradiation, STF not only

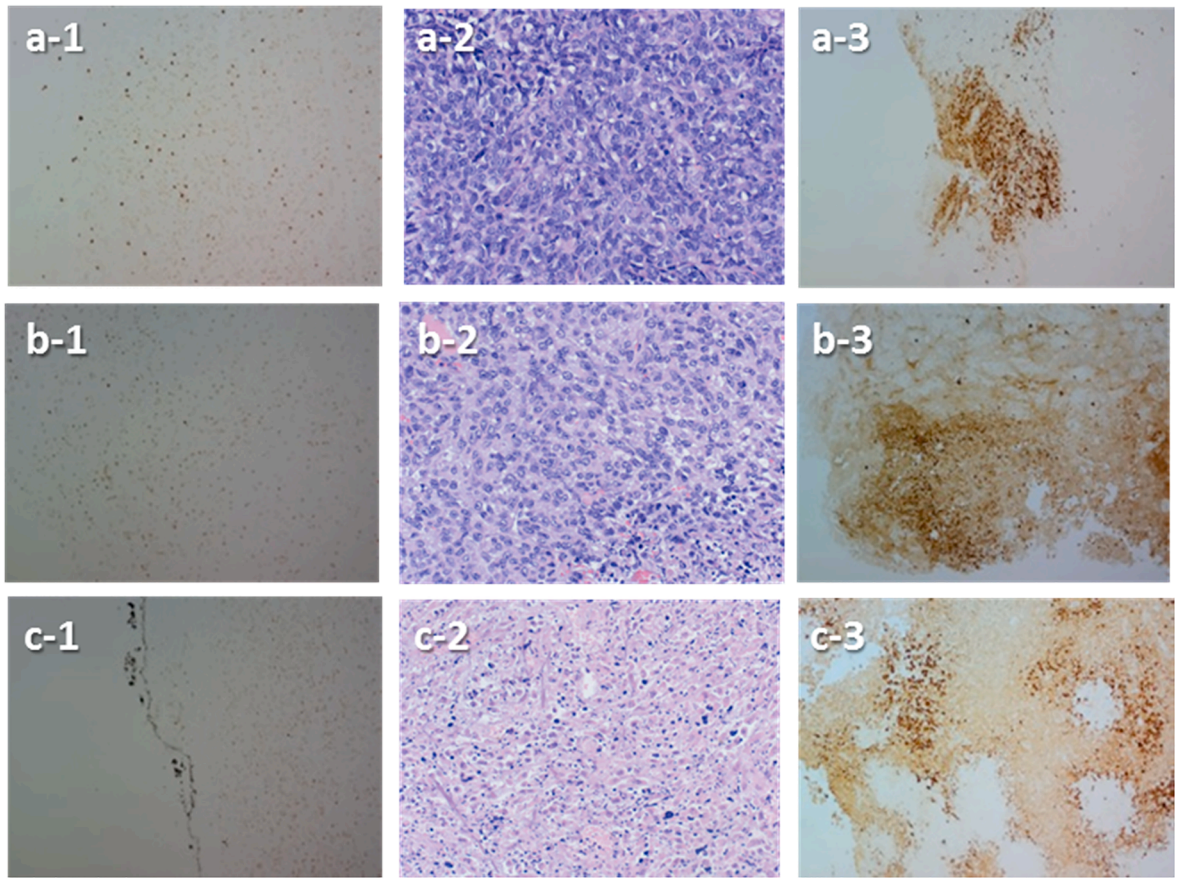

Fig. 10. The histological stain analysis of (□-1) KI67, (□-2) HE, and (□-3) Caspase 3 protein in the tumor of sacrificed mice in (a-□) control group, STF group (b-□) without and (c-□) with irradiation.

retained the heat on the tumor site, causing the localized hyperthermia, but also provided charge carriers derived ROS, further inducing tumor cell apoptosis. In summary, STF triggered by xenon irradiation showed efficient photothermal conversion, and subsequently contributing to the significant tumor ablation.

4. Conclusion

Through the one-pot hydrothermal synthesis and optimal calcination, the preferred crystal structure, morphology, and Ag self-precipitation effect were controllable in the Ag-doped TiO_2 photocatalysts. Among them, STF presented the superior photocatalytic activity, and rich electrons generation during the photo-induced reaction were observed, which was identified by ROS detection. Under the Xe lamp irradiation, 10,000 ppm of STF showed significant enhancement on the temperature in the photothermal conversion in vitro and photothermal therapy in vivo. The body surface temperature can be increased up to 47.96 °C with an irradiation time of 5 min. It was indicated that STF inhibited tumor growth by thermal ablation and extended the mice's survival rate. The protein identification by HE and Caspase 3 stain also revealed STF proficiently disturbed the tumor expansion and led to tumor cell apoptosis. In summary, STF can be triggered by Xe lamp irradiation and further presented efficient photothermal conversion, and subsequently contributing to the significant tumor ablation.

CRediT authorship contribution statement

Ting-Han Lin: Conceptualization, Methodology, Writing - original draft. **Ming-Chung Wu:** Writing - review & editing, Project administration, Funding acquisition, Supervision. **Yen-Ting Lin:** Data curation, Visualization, Investigation. **Chi-Hui Tsao:** Validation, Formal analysis, Investigation. **Yin-Hsuan Chang:** Visualization, Writing - review & editing. **Kou-Ping Chiang:** Resources, Investigation. **Yu-Ting Huang:** Investigation. **Yu-Jen Lu:** Methodology, Project administration, Funding acquisition.

Declaration of Competing Interest

The authors declare that they have no known competing financial interests or personal relationships that could have appeared to influence the work reported in this paper.

Acknowledgments

The authors appreciate Dr. Ming-Tao Lee (BL-13A1) and Dr. Jyh-Fu Lee (BL-17C1) at the National Synchrotron Radiation Research Centre for useful discussion and suggestions. We also thank Y.-M. Chang at the Instrumentation Centre of National Tsing Hua University for the TEM microstructure analysis.The financial support from the Ministry of Science and Technology, Taiwan (Project No. 108-2119-M-002-005, 109-2221-E-182-059, and 109-3116-F-002-002-CC2), Chang Gung University (QZRPD181), and Chang Gung Memorial Hospital, Linkou (CMRPD2H0173 and BMRPC74) are highly appreciated.

Appendix A. Supplementary material

Supplementary data to this article can be found online at https://doi.org/10.1016/j.apsusc.2021.149428.

References

[1] https://www.breastcancer.org/symptoms/understand_bc/statistics.
[2] N. Fernandes, C.F. Rodrigues, A.F. Moreira, I.J. Correia, Overview of the application of inorganic nanomaterials in cancer photothermal therapy, Biomater. Sci. 8 (2020) 2990–3020.
[3] C. Murugan, V. Sharma, R.K. Murugan, G. Malaimegu, A. Sundaramurthy, Two-dimensional cancer theranostic nanomaterials: synthesis, surface functionalization and applications in photothermal therapy, J. Controlled Release 299 (2019) 1–20.
[4] Y. Liu, P. Bhattarai, Z. Dai, X. Chen, Photothermal therapy and photoacoustic imaging via nanotheranostics in fighting cancer, Chem. Soc. Rev. 48 (2019) 2053–2108.
[5] W. Fan, B. Yung, P. Huang, X. Chen, Nanotechnology for multimodal synergistic cancer therapy, Chem. Rev. 117 (2017) 13566–13638.
[6] M. Wang, J. Song, F. Zhou, A.R. Hoover, C. Murray, B. Zhou, L. Wang, J. Qu, W. R. Chen, NIR-triggered phototherapy and immunotherapy via an antigen-capturing nanoplatform for metastatic cancer treatment, Adv. Sci. 6 (2019) 1802157.
[7] S. Liang, X. Deng, Y. Chang, C. Sun, S. Shao, Z. Xie, X. Xiao, P.A. Ma, H. Zhang, Z. Cheng, J. Lin, Intelligent hollow Pt-CuS janus architecture for synergistic catalysis-enhanced sonodynamic and photothermal cancer therapy, Nano Lett. 19 (2019) 4134–4145.
[8] Q. Tian, J. Hu, Y. Zhu, R. Zou, Z. Chen, S. Yang, R. Li, Q. Su, Y. Han, X. Liu, Sub-10 nm Fe_3O_4@$Cu_{2-x}S$ Core-shell nanoparticles for dual-modal imaging and photothermal therapy, J. Am. Chem. Soc. 135 (2013) 8571–8577.
[9] X. Huang, S. Tang, X. Mu, Y. Dai, G. Chen, Z. Zhou, F. Ruan, Z. Yang, N. Zheng, Freestanding palladium nanosheets with plasmonic and catalytic properties, Nat. Nanotechnol. 6 (2011) 28–32.
[10] X. Zhu, W. Feng, J. Chang, Y.-W. Tan, J. Li, M. Chen, Y. Sun, F. Li, Temperature-feedback upconversion nanocomposite for accurate photothermal therapy at facile temperature, Nat. Commun. 7 (2016) 10437.
[11] X. Cheng, R. Sun, L. Yin, Z. Chai, H. Shi, M. Gao, Light-triggered assembly of gold nanoparticles for photothermal therapy and photoacoustic imaging of tumors in vivo, Adv. Mater. 29 (2017) 1604894.
[12] M. Huo, L. Wang, Y. Wang, Y. Chen, J. Shi, Nanocatalytic tumor therapy by single-atom catalysts, ACS Nano 13 (2019) 2643–2653.
[13] R. Xing, Q. Zou, C. Yuan, L. Zhao, R. Chang, X. Yan, Self-assembling endogenous biliverdin as a versatile near-infrared photothermal nanoagent for cancer theranostics, Adv. Mater. 31 (2019) 1900822.
[14] W. Ren, Y. Yan, L. Zeng, Z. Shi, A. Gong, P. Schaaf, D. Wang, J. Zhao, B. Zou, H. Yu, G. Chen, E.M.B. Brown, A. Wu, A near infrared light triggered hydrogenated black TiO_2 for cancer photothermal therapy, Adv. Healthcare Mater. 4 (2015) 1526–1536.
[15] Z. Hou, K. Deng, M. Wang, Y. Liu, M. Chang, S. Huang, C. Li, Y. Wei, Z. Cheng, G. Han, A.A. Al Kheraif, J. Lin, Hydrogenated titanium oxide decorated upconversion nanoparticles: facile laser modified synthesis and 808 nm near-infrared light triggered phototherapy, Chem. Mater. 31 (2019) 774–784.
[16] S.-H. Chen, S.-H. Chan, Y.-T. Lin, M.-C. Wu, Enhanced power conversion efficiency of perovskite solar cells based on mesoscopic Ag-doped TiO_2 electron transport layer, Appl. Surf. Sci. 469 (2019) 18–26.
[17] N. Tsvetkov, A. Nikolskaia, O. Shevaleevskiy, S. Kozlov, M. Vildanova, B.C. Moon, J.K. Kang, L. Larina, TiO_2/halide perovskite interface: the impact of surface state passivation on energy alignment and photovoltaic performance of perovskite solar cells, Appl. Surf. Sci. 512 (2020) 145666.
[18] N. Kaliwoh, J.-Y. Zhang, I.W. Boyd, Characterisation of TiO_2 deposited by photo-induced chemical vapour deposition, Appl. Surf. Sci. 186 (2002) 241–245.
[19] M.S. Nasir, G. Yang, I. Ayub, S. Wang, W. Yan, In situ decoration of g-C_3N_4 quantum dots on 1D branched TiO_2 loaded with plasmonic Au nanoparticles and improved the photocatalytic hydrogen evolution activity, Appl. Surf. Sci. 519 (2020) 146208.
[20] N.K.A. Hamed, M.K. Ahmad, N.H.H. Hairom, A.B. Faridah, M.H. Mamat, A. Mohamed, A.B. Suriani, N. Nafarizal, F.I.M. Fazli, S.M. Mokhtar, W.I.W. Omar, M. Shimomura, Dependence of photocatalysis on electron trapping in Ag-doped flowerlike rutile-phase TiO_2 film by facile hydrothermal method, Appl. Surf. Sci. 534 (2020) 147571.
[21] E. Assayehegn, A. Solaiappan, Y. Chebude, E. Alemayehu, Fabrication of tunable anatase/rutile heterojunction N/TiO_2 nanophotocatalyst for enhanced visible light degradation activity, Appl. Surf. Sci. 515 (2020) 145966.
[22] G. Ou, Z. Li, D. Li, L. Cheng, Z. Liu, H. Wu, Photothermal therapy by using titanium oxide nanoparticles, Nano Res. 9 (2016) 1236–1243.
[23] M.-C. Wu, K.-C. Hsiao, Y.-H. Chang, S.-H. Chan, Photocatalytic hydrogen evolution of palladium nanoparticles decorated black TiO_2 calcined in argon atmosphere, Appl. Surf. Sci. 430 (2018) 407–414.
[24] M.-C. Wu, C.-H. Chen, W.-K. Huang, K.-C. Hsiao, T.-H. Lin, S.-H. Chan, P.-Y. Wu, C.-F. Lu, Y.-H. Chang, T.-F. Lin, K.-H. Hsu, J.-F. Hsu, K.-M. Lee, J.-J. Shyue, K. Kordás, W.-F. Su, Improved solar-driven photocatalytic performance of highly crystalline hydrogenated TiO_2 nanofibers with core-shell structure, Sci. Rep. 7 (2017) 40896.
[25] L. Lin, Z. Shi, J. Huang, P. Wang, W. Yu, C. He, Z. Zhang, Molecular adsorption properties of CH_4 with noble metals doped onto oxygen vacancy defect of anatase TiO_2 (1 0 1) surface: first-principles calculations, Appl. Surf. Sci. 514 (2020) 145900.
[26] G. Xu, Y. Zhang, D. Peng, D. Sheng, Y. Tian, D. Ma, Y. Zhang, Nitrogen-doped mixed-phase TiO_2 with controllable phase junction as superior visible-light photocatalyst for selective oxidation of cyclohexane, Appl. Surf. Sci. 536 (2021) 147953.
[27] L. Ling, Y. Feng, H. Li, Y. Chen, J. Wen, J. Zhu, Z. Bian, Microwave induced surface enhanced pollutant adsorption and photocatalytic degradation on Ag/TiO_2, Appl. Surf. Sci. 483 (2019) 772–778.
[28] M.-C. Wu, T.-H. Lin, K.-H. Hsu, J.-F. Hsu, Photo-induced disinfection property and photocatalytic activity based on the synergistic catalytic technique of Ag doped TiO_2 nanofibers, Appl. Surf. Sci. 484 (2019) 326–334.